

Origin of eclipsing time variations in Post-Common-Envelope binaries: role of the centrifugal force

Felipe H. Navarrete^{1*}, Dominik R.G. Schleicher², Petri J. Käpylä^{3,4}, Carolina Ortiz², and Robi Banerjee¹,

¹ Hamburger Sternwarte, Universität Hamburg, Gojenbergsweg 112, 21029 Hamburg, Germany

² Departamento de Astronomía, Facultad Ciencias Físicas y Matemáticas, Universidad de Concepción, Av. Esteban Iturra s/n Barrio Universitario, Casilla 160-C, Concepción, Chile

³ Institut für Astrophysik, Georg-August-Universität Göttingen, Friedrich-Hund-Platz 1, 37077 Göttingen, Germany

⁴ Nordita, KTH Royal Institute of Technology and Stockholm University, 10691 Stockholm, Sweden

Received –; accepted –

ABSTRACT

The eclipsing time variations in post-common-envelope binaries were proposed to be due to the time-varying component of the stellar quadrupole moment. This is suggested to be produced by changes in the stellar structure due to an internal redistribution of the angular momentum and the effect of the centrifugal force. We examine this hypothesis presenting 3D simulations of compressible magneto-hydrodynamics (MHD) performed with the PENCIL CODE, modeling the stellar dynamo for a solar mass star with angular velocities of 20 and 30 times solar. We include and vary the strength of the centrifugal force, comparing with reference simulations without the centrifugal force and including a simulation where its effect is enhanced. The centrifugal force is causing perturbations in the evolution of the stars, so that the outcome in the details becomes different as a result of non-linear evolution. While the average density profile is unaffected by the centrifugal force, a relative change in the density difference between high altitudes and the equator of order $\sim 10^{-4}$ is found. The power spectrum of the convective velocity is found to be more sensitive to the angular velocity than the strength of the centrifugal force. The quadrupole moment of the stars includes a fluctuating and a time-independent component, which varies with the rotation rate. As very similar behavior is produced in the absence of the centrifugal force, we conclude that it is not the main ingredient for producing the time-averaged quadrupole moment of the star. In a real physical system, we thus expect contributions from both components, that is, due to the time-dependent gravitational force from the variation in the quadrupole term and due to spin-orbit coupling due to the persistent part of the quadrupole.

Key words. magnetohydrodynamics – dynamo – methods: numerical – binaries: eclipsing

1. Introduction

Eclipsing time variations have been observed in a wide range of post-common-envelope binaries (PCEBs) (Zorotovic & Schreiber 2013; Bours et al. 2016). Traditionally, two explanations have been proposed for the observed variations: One refers to the possible presence of a third body, preferentially with high mass and on a wide orbit, which could explain the observed eclipsing time variations due to the orbit of the binary system around the common center of mass via the light travel time effect (e.g. Beuermann et al. 2012, 2013). The presence of such planets could in principle be explained either in case of surviving the common-envelope event (Völschow et al. 2014) or through their formation from the ejecta of common-envelope material (Schleicher & Dreizler 2014). However, the planetary systems were sometimes found to be unstable (Mustill et al. 2013), or the predicted planets have not been found (Hardy et al. 2015).

The alternative possibility is that the eclipsing time variation is caused in the binary system itself, as a result of magnetic activity. The latter could happen in different forms; an early suggestion by Decampli & Baliunas (1979) considered a rocket effect produced by anisotropic mass loss, though at the end rejected the hypothesis. Tidal torques are another possibility, but their magnitudes are so low (Zahn & Bouchet 1989) that they cannot transfer the necessary angular momentum (Applegate & Pat-

erson 1987). As a different solution, both Matese & Whitmire (1983) and Applegate & Patterson (1987) proposed that the orbital period would be changed if the stellar quadrupole moment changes as a result of magnetic activity.

This was a central step, though it remains important to identify what could cause the change of the stellar quadrupole moment and how strong it might be. In the original models (e.g. Matese & Whitmire 1983; Applegate & Patterson 1987), it was assumed that the magnetic field deforms the star by causing a deviation from its hydrostatic equilibrium, requiring thus a very strong magnetic field. Marsh & Pringle (1990) however showed that the required deformation was too strong to be produced by the luminosity of the star. A different scenario thus emerged, where the change of the quadrupole moment is not caused directly by the magnetic field, but as a result of angular momentum redistribution inside the star due to the dynamo process, leading then to stellar distortions as a result of the centrifugal force (Applegate 1992). Within a simplified thin-shell model, considering an inner core and an infinitely thin shell, Applegate (1992) calculated the quadrupole moment of the shell as

$$Q = \frac{1}{9} M_s R^2 \left(\frac{\Omega^2 R^3}{GM} \right), \quad (1)$$

where M is the mass of the star, $M_s \ll M$ the mass of the shell, Ω the angular velocity of the shell and R the radius from the center of the star to the shell. Applegate (1992) calculated the angular

* felipe.navarrete@hs.uni-hamburg.de

momentum to be transferred to produce a period variation ΔP as

$$\Delta J = -\frac{GM^2}{R} \left(\frac{a}{R}\right)^2 \frac{\Delta P}{6\pi}, \quad (2)$$

with a the separation of the binary system. The energy required to transfer the angular momentum is then

$$\Delta E = \Omega_{dr} \Delta J + \frac{(\Delta J)^2}{2I_{\text{eff}}}, \quad (3)$$

where Ω_{dr} refers to the difference of angular velocity between the shell and the core and I_{eff} is the effective moment of inertia, corresponding to about half of the inertial moment of the shell.

This model was extended by Brinkworth et al. (2006), considering a finite shell instead of an infinitely thin one, showing that the latter increased the energy required to produce the deformation by roughly one order of magnitude. Völschow et al. (2016) subsequently applied this model in a systematic way to the sample of Zorotovic & Schreiber (2013), showing that the energy requirement is sometimes fulfilled and sometimes not. A similar conclusion was obtained by Navarrete et al. (2018) through an extension of the analysis. On the other hand, more detailed 1D models solving the evolution equation for the stellar angular momentum indicated that the energetic requirement may actually be reduced (Lanza 2006), and Völschow et al. (2018) concluded that the mechanism is feasible for stars with masses of 0.3 – 0.36 M_{\odot} .

Other types of solutions have also been proposed; for instance Applegate (1989) derived librating and circulating solutions in the presence of a constant quadrupole moment, though these were originally predicted to provide modulations over shorter periods than observed in the PCEBs. Lanza (2020) however re-examined this scenario and proposed that a persistent non-axisymmetric internal magnetic field could produce an appropriate quadrupole moment to explain the observed deviations, at a much lower energetic expense than the scenario where the quadrupole moment variation is produced via the centrifugal force (e.g. Applegate 1992).

3D magneto-hydrodynamical simulations have recently investigated this problem, and in spite of not including the centrifugal force, they found quasi-periodic quadrupole moment variations caused by magnetic activity, though roughly still one order of magnitude lower than required by observations (Navarrete et al. 2020). As they were however not driven via the centrifugal force, it seems more likely that a change in the internal circulation in the star rather than a redistribution of the angular momentum has caused this result. This was recently confirmed via an even larger set of simulations with a more detailed analysis (Navarrete et al. 2021).

As the correct mechanism to give rise to the eclipsing time variations is still not established, it is however fundamental to investigate how the centrifugal force influences the change of the quadrupole moment within the stars. For this purpose, here we present and pursue 3D magneto-hydrodynamical simulations of a solar mass star that include and vary the centrifugal force, to assess in this way how it affects the stellar structure. In this way, we aim to verify if the origin of these variations is based on the centrifugal force as proposed by Applegate (1992), or if other mechanisms must be at play to cause the observed variations. Our numerical approach is presented in section 2, and the results are given in section 3. We finally present our discussion and conclusions in section 4.

2. Model

We present two sets of simulations with rotation rates $20\Omega_{\odot}$, and $30\Omega_{\odot}$, where Ω_{\odot} is the solar rotation rate. These are part of an overall larger set of simulations which has been pursued to analyze dynamos in the context of young stars (Navarrete et al., in prep.). We label the first set as the simulation group C and the second set as group D. Within each set, we vary the centrifugal force amplitude.

The compressible magnetohydrodynamics equations are solved on a spherical grid with coordinates (r, θ, ϕ) where $0.7 \leq r \leq R$ is the radial coordinate, where R is the radius of the star, $\pi/12 \leq \theta \leq 11\pi/12$ is the latitude, and $0 \leq \phi < 2\pi$ is the longitude. The model is the same as in Käpylä et al. (2013) and Navarrete et al. (2020, 2021). The equations are solved in the following form:

$$\frac{\partial \mathbf{A}}{\partial t} = \mathbf{u} \times \mathbf{B} - \eta \mu_0 \mathbf{J}, \quad (4)$$

$$\frac{D \ln \rho}{Dt} = -\nabla \cdot \mathbf{u}, \quad (5)$$

$$\frac{D \mathbf{u}}{Dt} = \mathcal{F}^{\text{grav}} + \mathcal{F}^{\text{Cor}} + \mathcal{F}^{\text{cent}} - \frac{1}{\rho} (\nabla p - \mathbf{J} \times \mathbf{B} - \nabla \cdot 2\nu \rho \mathbf{S}), \quad (6)$$

$$T \frac{D s}{Dt} = \frac{1}{\rho} [\eta \mu_0 \mathbf{J}^2 - \nabla \cdot (\mathbf{F}^{\text{rad}} + \mathbf{F}^{\text{SGS}})] + 2\nu \mathbf{S}^2, \quad (7)$$

where \mathbf{A} is the magnetic vector potential, $\mathbf{B} = \nabla \times \mathbf{A}$ is the magnetic field, \mathbf{u} is the velocity field, η is the magnetic diffusivity, μ_0 is the vacuum permittivity, \mathbf{J} is the current density, ρ is the density, p is the pressure, ν is the viscosity, \mathbf{S} is the rate of strain tensor, T is the temperature, s is the entropy. \mathbf{F}^{rad} and \mathbf{F}^{SGS} are the radiative and the subgrid scale flux, respectively (see e.g. Käpylä et al. 2013). Furthermore,

$$\mathcal{F}^{\text{grav}} = -(GM/r^2) \hat{r}, \quad (8)$$

$$\mathcal{F}^{\text{Cor}} = -2\Omega_0 \times \mathbf{u}, \quad (9)$$

$$\mathcal{F}^{\text{cent}} = -c_f \Omega_0 \times (\Omega_0 \times \mathbf{r}), \quad (10)$$

are the gravitational, Coriolis, and centrifugal forces. The parameter c_f was introduced by Käpylä et al. (2020) and controls the strength of the centrifugal force. $c_f = 1$ corresponds to the unaltered centrifugal force amplitude, and $c_f = 0$ implies no centrifugal force. It is defined as

$$c_f = \frac{|\mathcal{F}^{\text{cent}}|}{|\mathcal{F}_0^{\text{cent}}|} \quad (11)$$

with $\mathcal{F}_0^{\text{cent}}$ being the physically consistent magnitude of the centrifugal force. The need to control the centrifugal force arises due to the enhanced luminosity and rotation rate in simulations of stellar (magneto-) convection, an approach that is necessary to avoid a too large gap between acoustic, convective and thermal relaxation timescales in the simulations, as these are an essential ingredient for the modeling of the stellar dynamos (e.g. Brandenburg et al. 2005; Käpylä et al. 2013). The enhancement of the luminosity is described by a factor

$$\mathcal{L}_r = \frac{\mathcal{L}_{\text{sim}}}{\mathcal{L}_*}, \quad (12)$$

where \mathcal{L}_{sim} is the luminosity at the bottom of our model and \mathcal{L}_* is the luminosity at the bottom of the target, physical star. We

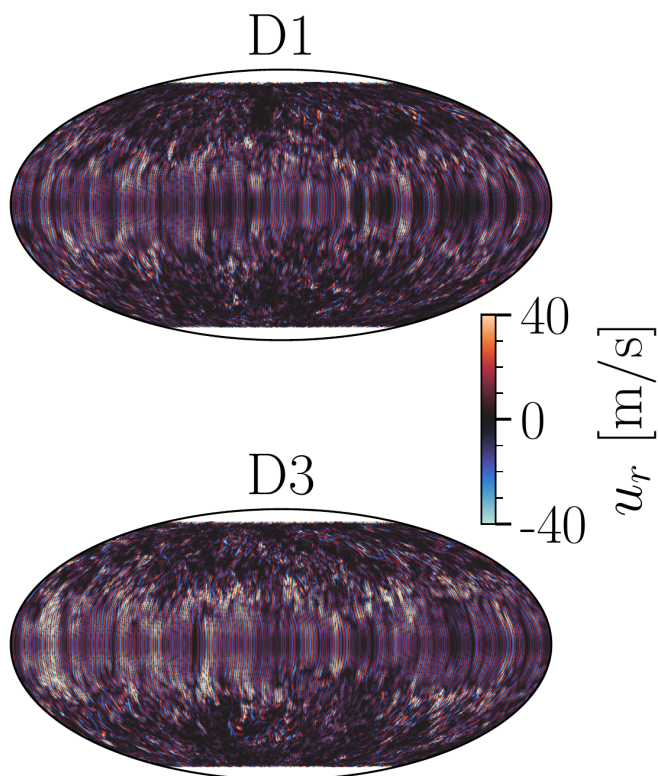


Fig. 1. Mollweide projections of radial velocity near the surface for runs D1 and D3.

have $\mathcal{L}_r = 8.07 \times 10^5$ for the setup adopted here for a Solar-like target star (Navarrete et al. 2020). The angular velocity has to be correspondingly enhanced to produce a realistic Coriolis number. For the centrifugal force, on the other hand, the strength should be limited to its physically expected value to not overestimate the impact on the structure of the star. For numerical stability and as outlined by Käpylä et al. (2020), each run is initialized with $c_f = 0$, and it is increased in small incremental steps after the saturated regime is reached. In this way, the effect of the centrifugal force can be explored in the simulation.

To quantify the strength of the centrifugal force, we compute the ratio of gravitational to centrifugal forces in the simulations presented here as well as for a real Sun-like star with the same rotation rate. The ratio of the two is defined as

$$\mathcal{F} = \frac{(|\mathcal{F}^{\text{cent}}|/|\mathcal{F}^{\text{grav}}|)_{\text{sim}}}{(|\mathcal{F}^{\text{cent}}|/|\mathcal{F}^{\text{grav}}|)_{\star}}, \quad (13)$$

where the subscripts \star denote the real star and *sim* the simulations. If this ratio is equal to unity, it basically means that the relative strength of the centrifugal force with respect to gravity is the same in the simulation as in the real star. Particularly for rapidly rotating stars, it is in principle harder to model a case with $\mathcal{F} = 1$ and we will typically stay somewhat below that ratio, though we also present a case with $\mathcal{F} > 1$ for comparison.

The details of the model were outlined further by Navarrete et al. (2020, 2021) and Käpylä et al. (2013) and we aim to avoid here too much repetition. We nonetheless recall that the model assumes an outer spherical boundary at the stellar radius which is assumed to be impenetrable and stress-free. At the lower boundary at 70% of the stellar radius, the magnetic field is assumed to obey a perfect conductor boundary condition, while at the top boundary the field is assumed to be radial. The temperature gradient is fixed at the bottom while blackbody condition is applied

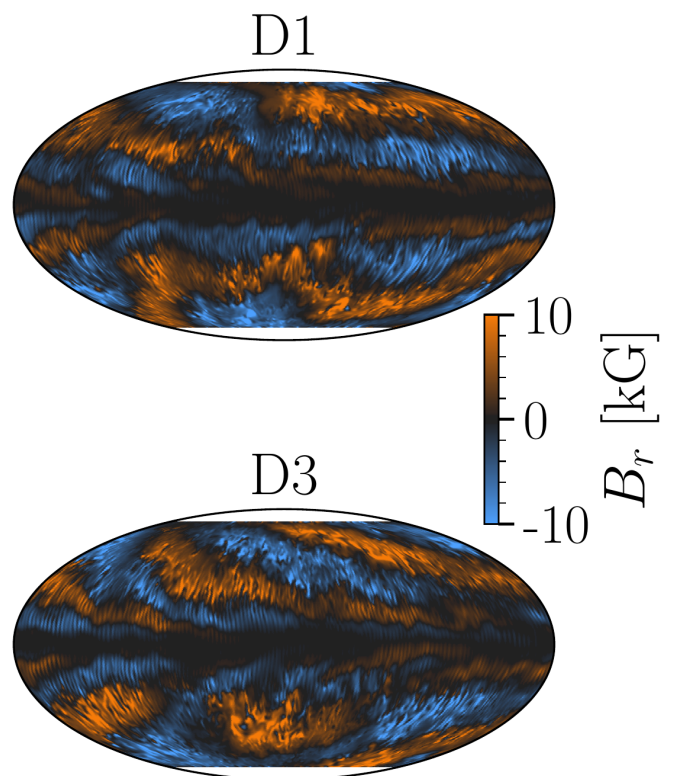


Fig. 2. Mollweide projections of radial magnetic field near the surface for runs D1 and D3.

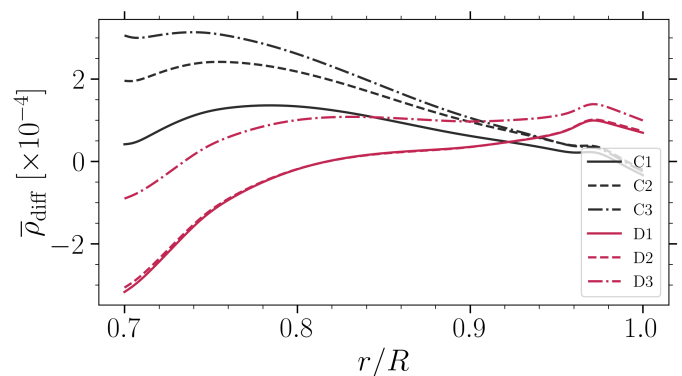


Fig. 3. Density difference between regions at 60° above the equator and the equator.

at the surface. The set-up includes latitudinal boundaries at 15° and 165° , where the plasma is assumed to be stress-free and perfectly conducting. Density and entropy are assumed to have zero first derivatives on latitudinal boundaries. The gravitational potential is spherically symmetric and time-independent, and self-gravity is not taken into account.

3. Results

We present the results of six simulations with different rotation rates and centrifugal force amplitudes. In the runs C, the rotation rate corresponds to 20 times solar and we consider $\mathcal{F} = 0, 0.875$, where we present two realizations of the second case. These are runs C2 and C3. In the series of runs D, the rotation rates is 30 times solar and we consider the cases $\mathcal{F} = 0, 0.875, 8.75$, which we label as D1, D2, and D3. The last simulation of this series is

Table 1. Summary of dimensionless parameters that characterize the simulations.

Run	Ω/Ω_\odot	c_f	Co	Ta	Re	Re_M	Pe	$\langle \Delta_\Omega^{(r)} \rangle_t$	$\langle \Delta_\Omega^{(60^\circ)} \rangle_t$	\mathcal{F}
C1	20	0	57.2	2.53(9)	22.1	22.1	55.3	9.46(-4)	3.43(-3)	0
C2	20	1.0(-4)	55.6	2.53(9)	22.8	22.8	57.0	9.67(-4)	3.44(-3)	8.75(-1)
C3	20	1.0(-4)	56.7	2.53(9)	22.3	22.3	55.8	8.71(-4)	3.51(-3)	8.75(-1)
D1	30	0	137.9	5.72(9)	13.8	13.8	34.6	-2.56(-4)	4.40(-4)	0
D2	30	1.0(-4)	137.8	5.72(9)	13.8	13.8	34.8	-2.60(-4)	4.55(-4)	8.75(-1)
D3	30	1.0(-3)	130.1	5.72(9)	14.6	14.6	36.6	-2.34(-5)	9.16(-4)	8.75

Notes. Co is the Coriolis number, Ta is the Taylor number, Re and Re_M are the fluid and magnetic Reynolds number, Pe is the Péclet number. For each run $\text{Pr} = 60$, $\text{Pr}_M = 1$, and $\text{Pr}_{\text{SGS}} = 2.5$.

considered as an extreme case where we exaggerate the effect of the centrifugal force to show the corresponding implications. In general the runs with centrifugal force are obtained by forking the runs with no centrifugal force and including it when the simulation is already at a thermally relaxed, saturated regime. Runs C2 and C3 have the same c_f but were initialized from C1 at different times. This was done to test whether the initial magnetic state of the parent run alters the solution of the forked run. We define the Coriolis, Taylor, Reynolds, magnetic Reynolds, Prandtl, magnetic Prandtl, SGS Prandtl, and Péclet numbers as

$$\text{Co} = \frac{2\Omega_0}{u_{\text{rms}}k_1}, \quad \text{Ta} = \left[\frac{2\Omega_0(0.3R)^2}{\nu} \right]^2, \quad \text{Re} = \frac{u_{\text{rms}}}{\nu k_1}, \quad (14)$$

$$\text{Re}_M = \frac{u_{\text{rms}}}{\eta k_1}, \quad \text{Pr} = \frac{\nu}{\chi_m}, \quad \text{Pr}_M = \frac{\nu}{\eta}, \quad \text{Pr}_{\text{SGS}} = \frac{\nu}{\chi_{\text{SGS}}^m}, \quad (15)$$

$$\text{Pe} = \frac{u_{\text{rms}}}{\chi_{\text{SGS}}k_1}, \quad (16)$$

where u_{rms} is the root-mean-square velocity, $k_1 = 2\pi/0.3R$ is an estimation of the wavenumber of the largest convective eddies, and χ_{SGS}^m is the subgrid scale entropy diffusion at the middle of the convective region. Each run is characterized by $\text{Pr} = 60$, $\text{Pr}_M = 1$, and $\text{Pr}_{\text{SGS}} = 2.5$. The other quantities are shown in Table 1.

3.1. Dynamical state in the simulations

In our simulations, the azimuthally averaged density profile at the equatorial plane of the star is basically unaffected by the centrifugal force; the only change we see occurs at high altitudes. We focus here on relative density differences between the region 60° above the equator and the density profile at the equator, which we define via

$$\bar{\rho}_{\text{diff}} = \frac{\bar{\rho}(\theta = 60^\circ) - \bar{\rho}(\theta = 0^\circ)}{\langle \bar{\rho} \rangle_{r\theta}}, \quad (17)$$

where $\langle \bar{\rho} \rangle_{r\theta}$ is the mean density averaged over latitude and radius. In the context of the enhanced luminosity method, we recall that density differences scale as (Brandenburg et al. 2005; Käpylä et al. 2013; Navarrete et al. 2020)

$$\bar{\rho}_{\text{diff}} \propto \mathcal{L}_r^{2/3}, \quad (18)$$

This implies that we should multiply with a factor $\mathcal{L}_r^{-2/3}$ to obtain the expected density difference in a physical star. We calculate these density differences and average them over the last 80 years of the simulation. They are given in Fig. 3 as a function of radius. We find that these differences are more relevant in the interior of the star, at 70 – 80% of the stellar radius, where they

have a typical magnitude of the order 10^{-4} . These density variations show clear trends with the centrifugal force which tends to increase the density difference between higher altitudes and equator towards positive values.

Snapshots of the final state of the radial (convective) velocity near the surface of the star are given in Fig. 1 for simulations D1 and D3, which are representative also of the other runs within our set of simulations. The series of runs C and D correspond to fast rotators and as such the convective cells are very small towards mid- to high-latitudes, whereas near the equator they become elongated. This is a common phenomenon obtained in simulations of stellar convection (see e.g. Viviani et al. 2018) and is consistent with the Taylor-Produman balance. The result for D3 is very similar compared to D1, though not identical. While both runs were evolved until the same time, an identical result is not expected due to the non-linear dynamics and as the centrifugal force causes perturbations within the star. On the other hand, and even though in principle the strength of the centrifugal force is quite significant in run D3, the impact on the flow pattern appears to be relatively minor.

Similar projections, now for the radial component of the magnetic field, are presented in Fig. 2. In run D1 clear non-axisymmetric structures are present which extend all over each hemisphere. Comparing by eye with D3, the non-axisymmetric structures seem to be somewhat smaller, that is, an $m = 2$ mode is also present. The amplitude of B_r remains very similar.

We decompose the radial velocity field at the surface of selected runs and calculate the normalized convective power spectra as

$$P_{\text{kin}} = \frac{E_{\text{kin},l}}{\sum_l E_{\text{kin},l}}, \quad (19)$$

where $E_{\text{kin},l}$ is the kinetic energy of the l -th degree. This is shown in Fig. 4 where we plot P as a function of l up to $l_{\text{max}} = 288$. We see that the convective power peak is shifted towards higher rotation rates but the centrifugal force has no significant influence on it, even in the extreme case of Run D3.

In Fig. 5, we show the azimuthally averaged angular velocity normalized with the initial angular velocity for simulations with different rotation rates and with and without the centrifugal force. In the set D, where the angular velocity in general is higher, we find that stellar differential rotation is reduced compared with set C, which is expected for more rapidly rotating runs (e.g. Kitchatinov & Rüdiger 1995; Viviani et al. 2018). Measures of the radial and latitudinal differential rotation are shown in the 9th and 10th columns of Table 1. They are defined

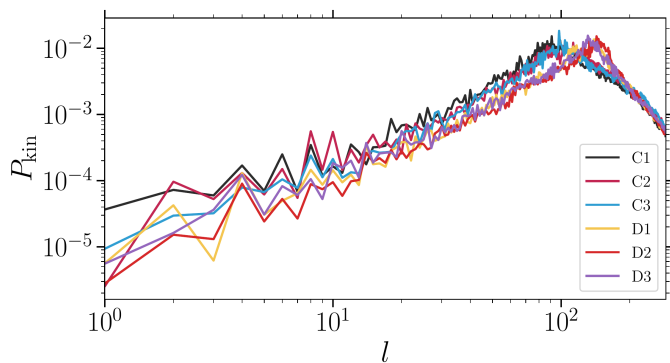


Fig. 4. Normalized convective power spectra for runs C1, C2, C3, D1, D2 and D3. The peak of convective power is shifted for higher rotation rates, while the centrifugal force seems to have no significant impact.

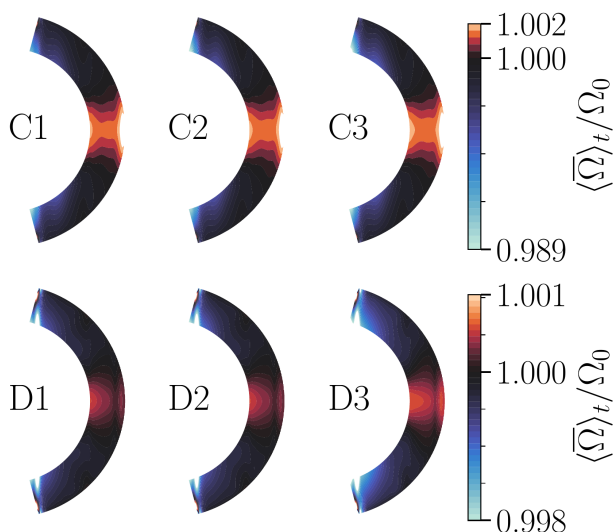


Fig. 5. Mean angular rotation rate averaged over the last 80 years of simulation and normalized to the angular rotation rate of the star.

as

$$\Delta_{\Omega}^{(r)} = \frac{\Omega_{\text{eq}} - \Omega_{\text{bot}}}{\Omega_{\text{eq}}}, \quad (20)$$

$$\Delta_{\Omega}^{(60^\circ)} = \frac{\Omega_{\text{eq}} - \Omega_{60^\circ}}{\Omega_{\text{eq}}}, \quad (21)$$

respectively. We see that the radial differential rotation remains practically the same within each set. The latitudinal differential rotation only changes appreciably in run D3 by a factor of two where we enhanced the centrifugal force. We do however not find strong evidence for a direct effect of the centrifugal force.

The magnetic field structure and its time evolution is clearly different in all simulations, and we also find differences in simulations with and without the centrifugal force. It is however difficult to assess whether that difference has an origin that is essentially related to a possible bi-modality of the solutions, or if the centrifugal force specifically introduces a different type of behaviour."

3.2. Gravitational quadrupole moment

We analyze the xx -component of the gravitational quadrupole moment for the runs C1, C2, C3 and D1, D2, D3. It is defined as

Table 2. Summary of the root mean square value and standard deviation of the quadrupole moment obtained in the simulations. Parenthesis indicate exponents of ten.

Run	rms [kg m^2]	σ [kg m^2]
C1	9.44(39)	2.19(39)
C2	8.25(39)	2.14(39)
C3	7.70(39)	2.08(39)
D1	1.76(40)	6.38(38)
D2	1.71(40)	5.94(38)
D3	1.02(40)	1.66(39)

$$Q_{ij} = I_{ij} - \frac{1}{3}\delta_{ij}\text{Tr}I, \quad (22)$$

where

$$I_{ij} = \int \rho(\mathbf{x})x_ix_jdV \quad (23)$$

is the inertia tensor with ρ being the density and x_i, x_j are Cartesian coordinates. The time evolution of Q_{xx} for all runs is shown in Fig. 7. Their yy - and zz -components evolve very similarly, as demonstrated in Navarrete et al. (2020). The average quadrupole moment and its standard deviation are summarized in Table 2 for each simulation.

For series C with the somewhat lower rotation rate, the average value of the quadrupole moment appears to be slightly less ($\sim 7-9 \times 10^{39} \text{ kg m}^2$) compared to series D ($\sim 1-2 \times 10^{40} \text{ kg m}^2$), while the standard deviation appears to be larger for series C ($\sim 2 \times 10^{39} \text{ kg m}^2$) compared to series D ($\sim 6-10 \times 10^{38} \text{ kg m}^2$). Within the range of uncertainty, both the mean value and the variation appear to be similar within the set of simulations C1, C2, C3, as well as within the set of simulations D1, D2, D3. This is to say that the centrifugal force does not appear to very strongly affect the mean while of the quadrupole moment. Concerning the standard deviation, it appears to be almost unaffected by the centrifugal force within the set C. Some more coherent variations are visible in run D2 and particularly in run D3 where the centrifugal force is the strongest of all runs. We note further that the drop of the mean quadrupole moment value in run D3 around $t = 100 \text{ yr}$ coincides with a decrease of the mean radial magnetic field around the same time that is visible in Fig. 6. Overall, the results thus indicate that the stellar quadrupole moment is not very sensitive to the centrifugal force.

4. Discussion and conclusions

We present here a series of numerical simulations investigating stellar dynamos of solar mass stars with angular velocities of 20 and 30 times solar rotation. The simulations have been performed using the enhanced luminosity method (Brandenburg et al. 2005; Käpylä et al. 2013; Navarrete et al. 2020) to avoid prohibitively large gaps in the relevant timescales. This entails the use of correspondingly enhanced rotation rates to ensure a realistic the Coriolis number in the simulations which is required to reach realistic magnitudes of drivers of dynamo action such as the α and Ω effects. We have included and varied the strength of the centrifugal force in these simulations, including cases without the centrifugal force or where the strength of the centrifugal force was enhanced by an order of magnitude.

The centrifugal force in general causes perturbations during the non-linear evolution, so that the models evolve differently in

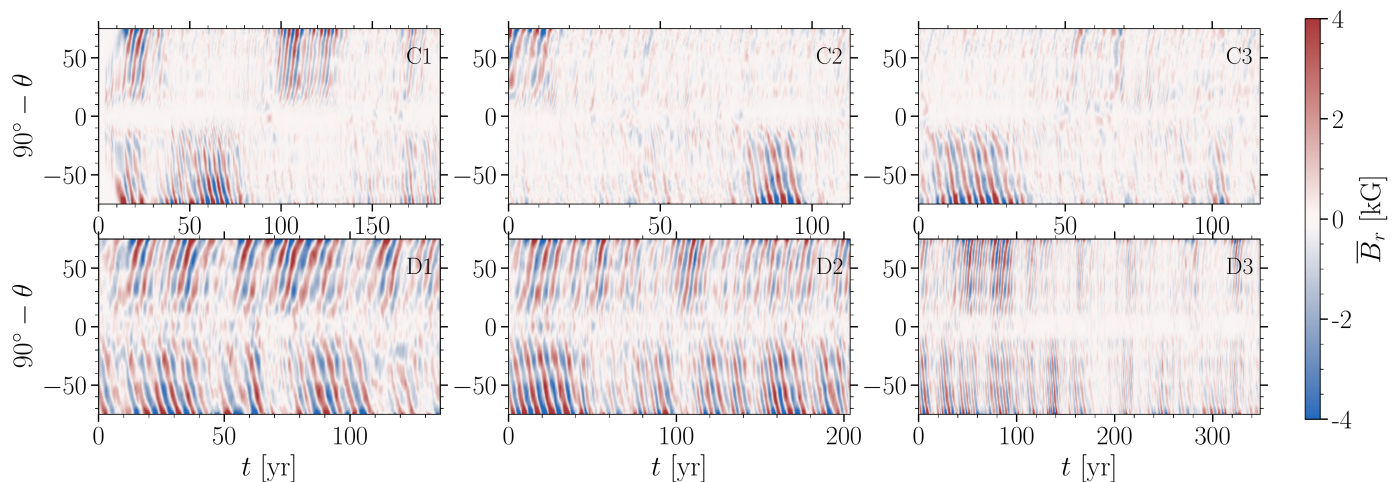


Fig. 6. Mean (azimuthally averaged) radial magnetic field near the surface for all runs.

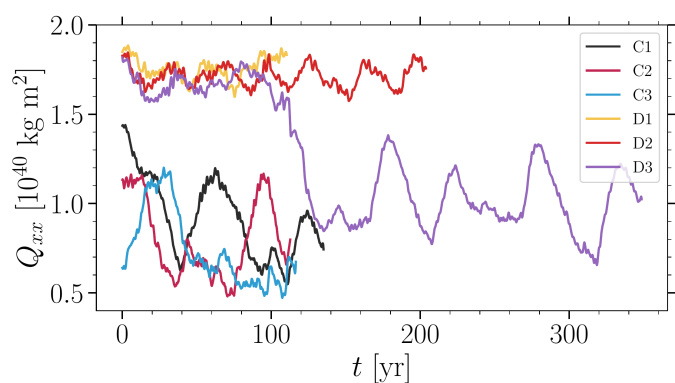


Fig. 7. Q_{xx} component of the gravitational quadrupole moment as a function of time for all runs.

the details, though it is hard to identify clear systematic effects. Particularly, we note that the averaged radial density profile of the stars remains almost unchanged, while the density difference between the equator and high altitudes (60°) changes by a relative amount of 10^{-4} . We see some difference between the distribution of axi-symmetric and non-axisymmetric modes of the dynamo, and the convective power spectra appear to be affected by the strength of the angular velocity, but not so much by the centrifugal force. Apart from the behavior of the density difference (Fig. 3) we do not see any clear systematic effects due to the centrifugal force.

Concerning the quadrupole moment, we similarly find that both its mean and its standard deviation depend more strongly on the angular velocity, while the influence of the centrifugal force is weak or almost non-existent, even in the simulation where the centrifugal force term is enhanced by an order of magnitude. This is highly relevant, as in the original models proposed by Applegate (1992), it was the centrifugal force term that was supposed to give rise to the variation of the stellar quadrupole moment, while here we find similar variations irrespective of the presence of the centrifugal force. This suggests that the centrifugal force plays only a minor role in causing this variation, as the overall flow patterns within the star are driven by more complex dynamics resulting from the non-linear evolution of the system. Adopting the parameters of V741 Tau (Völschow et al. 2016) and inserting the quadrupole variations that we find here into the framework of Applegate (1992) (see Navarrete et al. 2021),

we obtain period variations of the order of $10^{-8}\dots 10^{-9}$, whereas the amplitude of the period variation of close binaries is around $10^{-6}\dots 10^{-7}$ (see e.g. Völschow et al. 2018). While the original model was useful to motivate the possible origin of the fluctuations via magnetic activity, it overall appears to have difficulties to explain the observed magnitude of the variations and the centrifugal force is unlikely to be the main driver of the variations.

As in previous work (e.g. Navarrete et al. 2020, 2021), our simulations confirm that magneto-hydrodynamical simulations of stellar dynamos naturally produce an evolution of the stellar quadrupole moment, including a varying as well as an approximately constant component. The time-varying component may be somewhat too small to really explain the observed eclipsing time variations, and as suggested in models by Applegate (1989) and Lanza (2020), a roughly constant component could be producing the variations due to spin-orbit coupling via libration or circulation (see also discussion in Navarrete et al. 2021). As our simulations indeed show the presence of a mean and a fluctuating part of the quadrupole moment, the observed real variation may well consist of a superposition of both components, where the relative strength may depend on the specific system and its parameters. As demonstrated already by Navarrete et al. (2020), the presence of magnetic fields is crucial, as purely hydrodynamic simulations only produce short-term variations on the sound-crossing timescale of the star, but no longer-term variations on timescales of years or decades.

From the results obtained here, we overall thus conclude that neither the thin-shell model by Applegate (1992) nor the finite-shell model by Brinkworth et al. (2006) correctly describe the origin of the quadrupole moment variation, as they both assume it to originate from the centrifugal force and an internal re-distribution of the angular velocity, while in our simulations a change of the centrifugal force term does not lead to any appreciable change in the mean or fluctuating component of the quadrupole. The physics causing these variations thus require the modeling of the stellar dynamo with compressible MHD in 3 dimensions.

Acknowledgements. FHN acknowledges financial support from the DAAD (Deutscher Akademischer Austauschdienst; code 91723643) for his doctoral studies. DRGS gratefully acknowledges support by the ANID BASAL projects ACE210002 and FB210003, as well as via the Millennium Nucleus NCN19-058 (TITANs). DRGS and CO thank for funding via Fondecyt Regular (project code 1201280). PJK acknowledges financial support by the Deutsche Forschungsgemeinschaft Heisenberg programme (grant No. KA 4825/4-1).

References

- Applegate, J. H. 1989, *ApJ*, 337, 865
Applegate, J. H. 1992, *ApJ*, 385, 621
Applegate, J. H. & Patterson, J. 1987, *ApJ*, 322, L99
Beuermann, K., Breitenstein, P., Debski, B., et al. 2012, *A&A*, 540, A8
Beuermann, K., Dreizler, S., & Hessman, F. V. 2013, *A&A*, 555, A133
Bours, M. C. P., Marsh, T. R., Parsons, S. G., et al. 2016, *MNRAS*, 460, 3873
Brandenburg, A., Chan, K. L., Nordlund, Å., & Stein, R. F. 2005, *Astronomische Nachrichten*, 326, 681
Brinkworth, C. S., Marsh, T. R., Dhillon, V. S., & Knigge, C. 2006, *MNRAS*, 365, 287
Decampli, W. M. & Baliunas, S. L. 1979, *ApJ*, 230, 815
Hardy, A., Schreiber, M. R., Parsons, S. G., et al. 2015, *ApJ*, 800, L24
Käpylä, P. J., Gent, F. A., Olsper, N., Käpylä, M. J., & Brandenburg, A. 2020, *Geophysical and Astrophysical Fluid Dynamics*, 114, 8
Käpylä, P. J., Mantere, M. J., Cole, E., Warnecke, J., & Brandenburg, A. 2013, *ApJ*, 778, 41
Kitchatinov, L. L. & Rüdiger, G. 1995, *A&A*, 299, 446
Lanza, A. F. 2006, *MNRAS*, 369, 1773
Lanza, A. F. 2020, *MNRAS*, 491, 1820
Marsh, T. R. & Pringle, J. E. 1990, *ApJ*, 365, 677
Matese, J. J. & Whitmire, D. P. 1983, *A&A*, 117, L7
Mustill, A. J., Marshall, J. P., Villaver, E., et al. 2013, *MNRAS*, 436, 2515
Navarrete, F. H., Käpylä, P. J., Schleicher, D. R. G., Ortiz, C. A., & Banerjee, R. 2021, arXiv e-prints, arXiv:2102.11110
Navarrete, F. H., Schleicher, D. R. G., Käpylä, P. J., et al. 2020, *MNRAS*, 491, 1043
Navarrete, F. H., Schleicher, D. R. G., Zamponi Fuentealba, J., & Völschow, M. 2018, *A&A*, 615, A81
Schleicher, D. R. G. & Dreizler, S. 2014, *A&A*, 563, A61
Viviani, M., Warnecke, J., Käpylä, M. J., et al. 2018, *A&A*, 616, A160
Völschow, M., Banerjee, R., & Hessman, F. V. 2014, *A&A*, 562, A19
Völschow, M., Schleicher, D. R. G., Banerjee, R., & Schmitt, J. H. M. M. 2018, *A&A*, 620, A42
Völschow, M., Schleicher, D. R. G., Perdelwitz, V., & Banerjee, R. 2016, *A&A*, 587, A34
Zahn, J. P. & Bouchet, L. 1989, *A&A*, 223, 112
Zorotovic, M. & Schreiber, M. R. 2013, *A&A*, 549, A95